Journal of Nuclear Medicine, published on February 1, 2018 as doi:10.2967/jnumed.117.203943

Concurrent Respiratory Motion Correction of Abdominal PET and DCE-MRI using a Compressed Sensing Approach

Niccolo Fuin[1], Onofrio A. Catalano[1], Michele Scipioni[1,2], Lisanne P.W. Canjels[3], David Izquierdo-Garcia[1], Stefano Pedemonte[1], Ciprian Catana[1].

[1]Athinoula A. Martinos Center for Biomedical Imaging, Department of Radiology, Massachusetts General Hospital and Harvard Medical School, Charlestown, MA, USA.

[2]Department of Information Engineering, University of Pisa, Pisa, Italy.

[3]Department of Biomedical Engineering, Eindhoven University of Technology, Eindhoven, The Netherlands.

Corresponding author:

Ciprian Catana

149 13th St, Charlestown, MA 02129

Athinoula A. Martinos Center for Biomedical Imaging

Massachusetts General Hospital and Harvard Medical School

E-mail: ccatana@nmr.mgh.harvard.edu, phone: +1 617 643 4885

Number of words: 5189

Short title: PET/DCE-MRI concurrent motion correction

Financial Support: Funding for this work was provided by NIH grant 5R01-EB014894.

Abstract

We present an approach for concurrent reconstruction of respiratory motion compensated abdominal DCE-MRI and PET data in an integrated PET/MR scanner. The MR and PET reconstructions share the same motion vector fields (MVFs) derived from radial MR data; the approach is robust to changes in respiratory pattern and do not increase the total acquisition time.

Methods: PET and DCE-MRI data of 12 oncological patients were simultaneously acquired for 6 minutes on an integrated PET/MR system after administration of 18 F-FDG and gadoterate meglumine. Golden-angle radial MR data were continuously acquired simultaneously with PET data and sorted into multiple motion phases based on a respiratory signal derived directly from the radial MR data. The resulting multidimensional dataset was reconstructed using a compressed sensing approach that exploits sparsity among respiratory phases. MVFs obtained using the full 6-minute ($MC_{6\text{-}min}$) and only the last 1 minute ($MC_{1\text{-}min}$) of data were incorporated into the PET reconstruction to obtain motion-corrected PET images and in an MR iterative reconstruction algorithm to produce a series of motion-corrected DCE-MRI images (moco_GRASP). The motion-correction methods ($MC_{6\text{-}min}$ and $MC_{1\text{-}min}$) were evaluated by qualitative analysis of the MR images and quantitative analysis of maximum and mean standardized uptake values (SUV_{max}, SUV_{mean}), contrast, signal-to-noise ratio (SNR) and lesion volume in the PET images.

Results: Motion-corrected $MC_{6\text{-}min}$ PET images demonstrated 30%, 23%, 34% and 18% increases in average SUV_{max}, SUV_{mean}, contrast and SNR, and an average 40% reduction in lesion volume with respect to the non-motion-corrected PET images. The changes in these figures of merit were smaller but still substantial for the MC 1-min protocol: 19%, 10%, 15% and 9% increases in average SUV max , SUV mean, contrast and SNR; and a 28% reduction in lesion volume.

Moco_GRASP images were deemed of acceptable or better diagnostic image quality with respect to conventional breath hold cartesian VIBE acquisitions.

Conclusion: We presented a method that allows the simultaneous acquisition of respiratory motion-corrected diagnostic quality DCE-MRI and quantitatively accurate PET data in an integrated PET/MR scanner with negligible prolongation in acquisition time compared to routine PET/DCE-MRI protocols.

Keywords: motion-correction; PET/MRI; DCE-MRI; compressed sensing.

Hybrid positron emission tomography and magnetic resonance imaging (PET/MR) scanners are innovative devices that allow the simultaneous acquisition of metabolic, anatomical and physiological data for research and clinical applications (*1*). For example, the uptake of ^{18}F-FDG (using PET) and changes in signal intensity after MR contrast administration (using dynamic contrast enhanced – MRI (DCE-MRI)) can be concurrently assessed in suspicious lesions. DCE-MRI is an integral part of abdominopelvic examinations being useful for tumor detection and characterization. For this purpose, images have to be acquired at multiple time points following the injection of the MR contrast agent. In current clinical protocols, T1-weighted MR data are acquired at each time point during 14-20 seconds breath-holds over a period of 2-6 minutes (*2*), which requires patient cooperation.

In addition to improving the patient experience by performing a one-stop-shop examination, integrated PET/MR scanners also have the potential to greatly improve the image quality by eliminating the issues related to patient repositioning and registration of separately acquired images. However, respiratory motion is still a major source of deterioration of image quality in PET and could be a cause of misregistration between PET and DCE-MRI images, as PET data is acquired during free-breathing (*3*). To control the effects of motion, the acquired PET data can be gated based on a respiratory signal obtained with an external device (e.g. pressure sensor mounted in a chest belt) (*4,5*). This technique, however, sacrifices SNR, as it only uses a small fraction of the emission events. Alternatively, motion compensation can be performed assuming that a respiratory signal and MVFs are available (*6*). Data-driven motion compensation techniques to obtain these from the PET data itself have been developed (*7,8*). Although useful in certain scenarios, these approaches are dependent on the counting statistics and spatial distribution of the radio-tracer in the body.

As an alternative, the simultaneous acquisition of MR data using hybrid PET/MR scanners offers the possibility to estimate the MVFs by non-rigidly co-registering a series of high temporo-spatial resolution MR images (*9*). Such a method is more robust than PET-based methods and has the advantage of being radio-tracer independent. Numerous techniques have been proposed for characterizing motion

using MR in the context of PET/MR (*10-15*). For example, the respiration model can be constructed from a series of 2D images repeatedly acquired over several respiratory cycles (*10,11*). Tagged MR, phase contrast MR and pulse field gradient methods can also be used to estimate the motion fields and have been used for MR-assisted PET motion correction (*12-15*). Although these approaches have been shown to lead to an improvement in PET image quality, they typically require several minutes of dedicated MR acquisition per bed position or employ a small number of motion phases, reduced spatial resolution, or restrict the registration to only two dimensions. Furthermore, these MR sequences are not useful for diagnostic purposes, thus requiring a change to the standard protocols to be able to collect the respiratory signal or MR-derived motion model in a clinical setting.

In order to foster clinical acceptance, the MR-based respiratory motion correction techniques must not increase the total acquisition time, be robust to changes in respiratory patterns during the whole scanning period, and provide MR images of diagnostic value. In an effort to meet these goals, the data acquired using a self-gated golden-angle 3D radial stack-of-stars MR spoiled Gradient Echo Sequence (radial_VIBE) (*16,17*) was proposed for motion correction of PET images (*18*). Radial schemes allow for respiratory self-gating to obtain the MVFs. In addition, the resulting static T1-weighted MR images provide diagnostic information (*19,20*). However, despite these advantages, the 6-10 min acquisition time of the data needed for motion modeling in (*18*), prevented the acquisition of other diagnostic MR data. When the acquisition time was reduced to under 2 minutes, streak artifacts appeared from azimuthal undersampling of the radial k-space trajectory. These artifacts decrease the quality of motion estimation and thus of the resulting motion-compensated PET and MR images if no artifact-resistant methods are applied (*21,22*).

Compressed Sensing (CS) reconstruction of the MR images (*21,22*), can help to highly increase the tolerance to undersampling streaking-artifact. In (*21,23*), the acquisition of a radial_VIBE MR sequence together with a CS reconstruction framework allowed the reconstruction of clinically useful DCE-MRI images of the abdomen. In (*24*) a motion signal was extracted from a radial_VIBE MR sequence and in (*25*) distinct motion phase images were obtained from a radial_VIBE DCE-MRI sequence.

In this work, building upon previously published methods (*21-25*), we aimed to demonstrate that it is possible to perform concurrent reconstruction of respiratory motion compensated DCE-MRI and PET data using MVFs derived from radial MR data using a CS approach. The same radial MR data is therefore used to obtain the respiratory signal, MVFs and motion compensated DCE-MRI images. Concurrent in this context was used to denote the fact that the same MVFs were used for both reconstructions and not that the data were jointly reconstructed.

Our second goal was to demonstrate that a respiratory motion model can also be obtained from a 1 minute radial_VIBE MR acquisition using a CS reconstruction. This allows the acquisition of other diagnostic MR data during PET/MR scans when a DCE-MRI is not required. As described above, this shorter MR sequence also allows us to obtain the respiratory motion signal and displacement fields to perform PET respiratory motion correction.

We investigated the feasibility and robustness of the two methods by performing a comparative study of the motion-corrected and uncorrected PET and of the obtained DCE-MRI images, assessing the differences in radio-tracer uptake quantification and lesion volume.

MATERIAL AND METHODS

Data Acquisition

PET and MR data were acquired simultaneously using the Biograph mMR scanner (Siemens Healthineers, Erlangen, Germany) as part of a study approved by the local Institutional Review Board. 12 patients with suspected malignant disease in the abdomen were enrolled in this study. Emission data were acquired 108±14 minutes (mean ± standard deviation) after administration of 351±20 MBq of ^{18}F-FDG. The data were acquired in 3D mode for 6 minutes after running a 2-point Dixon sequence to derive the attenuation map (μ-map) during end-expiration breath hold. Concurrently, the radial_VIBE using a golden-angle acquisition scheme (*16*) was run and, next, a conventional cartesian volumetric interpolated breath-hold examination (bh_VIBE)) sequence was also acquired. Relevant imaging parameters were: axial phase

encoding, repetition time / echo time (TR/TE) ≈ 3.75/1.7 ms, flip angle = 10, FOV = 400 × 400 × 258 mm^3, number of readout points in each spoke = 256, number of partitions = 56, with 15% slice resolution reduction and 6/8 partial Fourier applied along the slice dimension, resulting in a spatial resolution of 1.56 × 1.56 × 4.6 mm^3. The radial_VIBE sequence was acquired for 6 minutes during the entire PET acquisition. An intravenous injection of 10 mL of gadoterate meglumine (Dotarem, Guerbet LLC) was initialized 40 seconds after the start of the radial_VIBE data acquisition, followed by a 20-mL saline flush, both injected at a rate of 2 mL/s. The conventional bh_VIBE data were acquired 20 seconds after the end of the radial_VIBE acquisition, in the same bed position.

Respiratory Motion Signal Extraction and Data Binning

A respiratory motion signal was obtained from the radial_VIBE MR data. The stack-of-stars k-space trajectory allowed the derivation of a self-gating respiratory motion signal from the central k-space line (kx = ky = 0). Specifically, a projection profile was computed for each acquisition angle by taking a 1D partition-direction Fourier transform of the central k-space line. The projection profiles from all the RF coil elements were first concatenated. Next, principal component analysis was performed and the component with the highest peak in the frequency range of 0.1–0.5 Hz was selected (*24*). The DCE signal was estimated using a spline data fitting procedure and subtracted from the original signal (*25*). Spurious high frequency components were removed using a low pass filter.

Based on the respiratory signals, the MR k-space and the PET listmode data were subdivided into 6 respiratory bins using a variable amplitude based method. As opposed to traditional amplitude-based gating schemes, each bin generated using the variable amplitude-based binning approach contained an equal amount of data. This scheme ensured comparable statistics for both the MR raw and PET list-mode data. Because the variable amplitude-based binning could only be performed if PET and MR data acquisitions were fully synchronized, the MR sequence was modified to transmit a synchronization trigger into the PET list-mode stream at every pass through the center of the k-space.

Statistic MR Reconstruction of the Motion Phases

The volumes corresponding to the six respiratory phases were reconstructed from the radial_VIBE MR data. The reconstruction method we adopted was a combination of CS and parallel imaging, in a framework known as Golden-Angle Radial Sparse Parallel MR (GRASP) (*21*). In this specific implementation, we used a fully 3D graphics processing unit (GPU) based Non-Uniform Fast Fourier Transform (NUFFT) operator (*26,27*). As demonstrated in (*21*), GRASP enables robust reconstruction even in the presence of strong undersampling, thus suppressing artifacts such as streak or noise when the total number of radial planes decreases. In order to test the robustness of the method to shorter MR acquisition times we employed the full 6 minute radial_VIBE acquisition ($MC_{6\text{-}min}$) or only the 1 minute of data ($MC_{1\text{-}min}$) to generate the motion phases. The last minute of the acquisition was used, as in this time period, gadoterate meglumine was present in the tissues, providing better MR contrast with respect to, for example, the first minute of acquisition.

Based on the respiratory motion signal, a set of 6 × 400 ($MC_{6\text{-}min}$) and 6 × 66 ($MC_{1\text{-}min}$) radial k-space planes were generated and reconstructed using the GRASP framework. For comparison, both datasets were also non-iteratively reconstructed using only an inverse NUFFT operator (in the remaining of this manuscript, these reconstructions are named $MC_{6\text{-}ifft}$ and $MC_{1\text{-}ifft}$ respectively). The end-expiration phase was set as the reference phase; the other phase volumes were registered to the reference volume using a B-spline non-rigid image registration software (Elastix, UMC Utrecht, The Netherlands (*28*)) and corresponding MVFs were also obtained.

PET and MR Motion Corrected Reconstruction

The MVFs were employed by iterative reconstruction algorithms to obtain motion corrected DCE-MRI and PET images. These algorithms reconstructed iteratively the images at a given reference respiratory phase, accounting for the deformations at every iteration.

Reconstructions of 4D respiratory motion-resolved PET images were performed using a 4-D ordinary Poisson ordered subset expectation maximization (4D OP-OSEM) algorithm (*29*). The update equation of the vector of emission rates λ, at every iteration *n.* is defined as follows:

$$\lambda_i^{(n+1)} = \sum_x \left(\frac{\lambda_{i,t^x}^n}{\sum_d T_x' h_{id} c_d a_{dt^x}} \sum_d T_x' h_{id} \frac{v_{dt^x}}{\sum_j T_x h_{jd} \lambda_j^n + \frac{s_{dt^x}}{a_{dt^x}} + \frac{r_{dt^x}}{c_d a_{dt^x}}} \right) \qquad (1)$$

where the elements of the system matrix h_{id} represent the geometric probability that photons emitted from voxel *i* are detected in the line of response (LOR) *d*; v are the emission data; a_d are the attenuation factors; c_d are the detector normalization factors; s_d and r_d are the expected contributions of scatter and random coincidences respectively. Scatter distribution sinograms were calculated using an implementation of the single scatter simulation method with relative scaling, provided by the manufacturer. The standard OP-OSEM algorithm was extended to incorporate MVFs into the reconstruction process (*30,31*). The emission data, randoms, and attenuation correction factors are motion phase-dependent. T_x is defined as a transforming operation, mapping the volume of motion phase t^1 to t^x, applying the dedicated MVFs (*28*); and T_x' is the inverse transforming operation, mapping the volume of motion phase t^x to t^1. This algorithm reconstructed iteratively the image at a given reference respiratory phase, accounting for the deformations at every OSEM iteration. Each update of the image was obtained by warping the current image estimate according to the deformations at all respiratory phases, projecting the warped images (utilizing a warped μ-map), back-projecting the residuals of the projections and warping the resulting volumes back to the reference frame; the warped volumes were summed to form the new estimate of the activity. The 4-D MLEM algorithm naturally accounted for the deformation of the μ-map and the corrections for scatter and random coincidences. The 3-D static images, used for comparison, were obtained without including the transformation in the reconstruction. All the resulting images were post-smoothed using a Gaussian filter with a 4 mm kernel. The algorithm was implemented utilizing the GPU-based tomographic reconstruction software Occiput.io (*32*).

For the motion-corrected DCE-MRI reconstruction framework (moco_GRASP), the acquired golden angle dataset was sorted into multiple sets of undersampled data. The radial k-space data were sorted into 6 respiratory phases and 18 time bins. Similarly to the 4D OP-OSEM algorithm, the moco_GRASP algorithm accounted for the MVFs at every iteration. The MVFs were therefore directly included into the reconstruction framework that outputs a single MR image, at the reference phase, for every time bin. A Total Variation constraint was enforced along the contrast-enhancement (or time) dimension (*21*). The MR reconstruction cost-function was formulated as follows:

$$C(f) = \arg\min \left\| F \sum_{t} T_x B f - m \right\| + a|Zf|$$

where *F* is the NUFFT operator (*27*) defined for the radial sampling pattern; *B* represents the coil sensitivity map; *f* is the 4D dynamic image-series with an additional contrast-enhancement dimension; and *m* is the corresponding multi-coil radial k-space data sorted according to the four data dimensions; *T* is the transforming operation defined for equation 1; and *Z* is the sparsifying transform applied to the contrast-enhancement dimension with regularization parameter *α*. From the first term of equation 2, the following updated MRI image volume $f_x^{(i+1)}$ for motion phase *x* and iteration *(i +1)* can be derived:

$$f_x^{(i+1)} = f_x^i + \beta(F'T'_x\left(FT_x B f^i - m_x\right))$$

The obtained volumes for the 6 phases were summed, at every iteration, to form the new estimates of the DCE-MRI images $f^{(i+1)}$. This algorithm reconstructed iteratively the dynamic MR images at a given reference respiratory phase, employing 100% of the MR raw data.

Analysis of Impact of Motion Correction on PET and MR Image Quality and Quantification

Analysis of the MR Respiratory Phase Images Utilized to Generate MVFs. The MR volumes corresponding to the 6 respiratory phases were reconstructed using both the GRASP method and the inverse NUFFT operator from the 6- and 1-minute acquisitions. The images were first qualitatively analyzed with a focus on the presence of streak artifacts. Next, the mean square errors (MSEs) were calculated, to compare

the images obtained using the reduced acquisition time and for the different reconstruction methods with the images obtained from the full 6-minute acquisition and using the GRASP reconstruction as reference.

PET Image Analysis. For each patient, MVFs estimated from the MR volumes corresponding to the 6 respiratory phases, resampled to the PET resolution and field of view, were used to generate motion-corrected PET images as explained in section 2.4. It is important to note that the various MVFs were applied to the same gated PET sinograms. The motion-corrected PET images were quantitatively compared to the uncorrected ones by assessing changes in SUVs in lesions that exhibited tracer uptake sufficient for unambiguous segmentation in all static, gated, and motion-corrected images. 18 lesions were identified and isocontour volumes of interest were segmented for each lesion individually by using a region-growing algorithm (isocontour threshold, 50%). The maximum SUV (SUV_{max}) and mean SUV (SUV_{mean}) in each isocontour volume of interest were calculated (*33*). Contrast (C), SNR and lesion volume were also calculated as described in (*8*). Image noise was obtained as the standard deviation in a cubical volume of interest defined in the liver excluding voxels at the edge or those with focal tracer uptake.

DCE-MRI Image Analysis. DCE-MRI data were obtained simultaneously with the PET data acquisition using the moco_GRASP reconstruction approach. A set of 18 pre- and post-contrast enhancement images were generated from the DCE_MRI data for every patient. The images corresponding to the baseline, early arterial, dominant arterial, portal venous, equilibrium and late phases were selected. A comparative analysis of the image quality obtained with the conventional bh_VIBE acquisition and moco_GRASP reconstruction was possible only for the late phase of contrast enhancement images, as bh_VIBE images were acquired 3560 seconds after contrast injection (20 s after the end of the radial_VIBE acquisition). The resulting images were visually evaluated by an accredited radiologist with 18 years of experience in clinical oncology.

RESULTS

Morphological MR Image Analysis

The MR images for the end-expiratory and end-inspiratory phases for patient 1 are shown in Supplemental Fig. 1. The MR images obtained from the 6-minute acquisition using GRASP reconstruction ($MC_{6\text{-min}}$) are presented in Supplemental Figs. 1A and 1B. The image quality for the 1-minute acquisition using GRASP reconstruction ($MC_{1\text{-min}}$) appeared stable, and only local artifacts were noticed visually in Supplemental Figs. 1C and 1D. A substantial decrease in image quality can be observed in the images reconstructed using the non-iterative method (Supplemental Figs. 1E and 1F). MSE for the different reduced scan times and for the different reconstruction methods, with respect to the full 6 min acquisition using GRASP reconstruction are given in Table 1. With a reduced scan time of 1 min and an inverse FFT reconstruction, strong deviations are introduced. With a scan time of 1 min and GRASP reconstruction, deviations are reduced by 70% but they still do not reach the same level of a 6 min acquisition with a simple inverse FFT reconstruction. It should be noted that differences in the deformation fields, used for PET motion correction, and obtained with $MC_{1\text{-min}}$ (with respect to $MC_{6\text{-min}}$) do not only originate from the increased artifact level, but may also be attributed to a change in the respiratory pattern, e.g., if the patient takes deeper breaths after injection of gadolinium. With a 1-minute acquisition the breathing pattern of the patient is not followed continuously and may not be captured in its full amplitude range.

Analysis of Motion Corrected PET Data

The PET images corresponding to three respiratory gates for a representative patient are shown in Fig. 1. The respiration-induced motion of the liver lesion in the cranio-caudal direction can be appreciated. Examples of the uncorrected and motion-corrected PET images using both motion correction protocols ($MC_{1\text{-min}}$ and $MC_{6\text{-min}}$) are given in Fig. 2. The improved sharpness when compared to the uncorrected images can be appreciated visually and from the line profile defined across the lesion (Fig. 2D). For this specific lesion, the peak SUV value was increased by 45% using $MC_{6\text{-min}}$ and 29% using $MC_{1\text{-min}}$. Similar images for a different patient are shown in Supplemental Figs. 2 and 3. The results of the quantitative analysis for all the patients are presented in the bar charts of Fig. 3. The motion-corrected $MC_{6\text{-min}}$ PET

images exhibited the highest SUV_{mean}, SUV_{max}, contrast and SNR, with average relative differences of $dSUV_{max}$ = 30%, dSUV_mean = 23%, dContrast = 34%, dSNR = 18% and dVolume = -40% with respect to the non-motion-corrected PET images. The motion-corrected $MC_{1\text{-}min}$ PET images also exhibited an improvement, with average relative differences of dSUV_max = 19%, dSUV_mean = 10%, dContrast = 15%, dSNR = 9% and dVolume = -28%. The $MC_{6\text{-}min}$ approach achieved a substantial improvement for all the examined quantitative measures compared to the ungated reconstruction and to the $MC_{1\text{-}min}$ protocol.

Analysis of Motion-Corrected DCE-MRI Data

Representative moco_GRASP DCE-MRI liver axial images are shown in Fig. 4 and Supplemental Fig. 4. Fig. 4A and Supplemental Fig. 4A show the non-contrast enhanced phase, Fig. 4B and Supplemental Fig. 4B show the arterial dominant phase and Fig. 4C and Supplemental Fig. 4C show the portal venous phase. Fig. 4D and Supplemental Fig. 4D show the corresponding motion-corrected PET image. All DCE-MRI and moco_GRASP images were deemed of diagnostic quality. Supplemental Fig. 5 shows two examples of late post-contrast images acquired with the moco_GRASP reconstruction method (Supplemental Figs. 5A and 5C) and with a conventional cartesian bh_VIBE (Supplemental Figs. 5B and 5D). From these examples, it can be noted that the MR images obtained with moco_GRASP are slightly less sharp than the images obtained from a bh_VIBE acquisition. However, the free-breathing moco_GRASP acquisition is robust to motion and does not present motion artifact that could occur when the patient is not capable to held breath during a 20-second bh_VIBE acquisition (as can be noted in Supplemental Fig. 5D).

DISCUSSION

Respiratory motion is one of the primary challenges in achieving unbiased measurements of lesion radiotracer concentration in abdominal PET imaging and a source of misregistration between the PET and DCE-MRI images even in simultaneous PET/MR imaging.

In this study, we proposed a method for concurrent reconstruction of respiratory motion compensated liver DCE-MRI and PET data. Using the proposed protocol ($MC_{6\text{-min}}$), the motion model is derived from a continuously acquired radial DCE-MRI data (*16*) and the different motion phases are reconstructed using a CS approach (*25*). The acquisition time of the DCE-MRI data that also allows the derivation of the respiratory motion model is similar to that of the current clinical protocol that requires a set of Cartesian bh_VIBE DCE-MRI acquisitions, but our approach follows continuously the breathing pattern of the patient during acquisition. To allow the derivation of the motion model while minimally modifying the clinical MR protocol even in those studies that do not require DCE-MRI, we also proposed a 1-minute data acquisition protocol for respiratory motion characterization that could be appended to routine examinations.

Improvements of PET image quality and quantification accuracy in terms of SUV_{max}, SUV_{mean}, contrast, and SNR were demonstrated in all 12 patients. These values were similar to those reported in previous studies (e.g. 12-19% SUV underestimation) (*8,18*) for the $MC_{1\text{-min}}$ protocol and even higher (up to 30%) for the $MC_{6\text{-min}}$ protocol. Impact on patient management, for a greater pool of patients, will be demonstrated in a future study. The better performance of the $MC_{6\text{-min}}$ protocol with respect to previously presented results (*8,10,11,18*), can be attributed to several factors related to the MR acquisition and to the adopted MR reconstruction method. The MR acquisition in $MC_{6\text{-min}}$ was 6 minutes long, yielding better SNR, improved sharpness and reduced streak artifacts in the MR images corresponding to the respiratory phases. The presented method follows continuously the respiratory pattern for the entire PET acquisition and produces a comprehensive motion model. Furthermore, for the first time, DCE-MRI images have been employed to obtain a motion model, allowing for a much better delineation of the lesion from the adjacent healthy tissue. The contrast enhancement, consequently, produced an improved motion model for the lesion itself. Finally, the use of iterative GRASP reconstruction (*21*) to obtain MR images of the motion phases helps to increase the tolerance to undersampling artifacts.

Building upon previously published methods (*21-25*), we also introduced a reconstruction method to obtain motion-corrected DCE-MRI images of the abdomen, from radial VIBE data. In (*25*), continuously acquired k-space data were sorted into multiple sets of undersampled datasets with distinct motion states, using motion signal extracted directly from DCE-MRI data (*24*). The motion phases were then reconstructed relying on the use of CS. In the work presented in this manuscript, MVFs are extracted from the reconstructed motion phases and subsequently included in a 4D MRI statistical reconstruction process to obtain motion corrected DCE-MRI images. The multiphase liver images were deemed of diagnostic quality by an accredited radiologist. Slightly lower image quality for the arterial compared with the venous phase was observed as previously reported in (*23*). This is likely related to increased streak artifacts from the rapid change in signal intensity in the aorta and liver from the arrival of the bolus of contrast, but, in all cases, images were considered as acceptable or qualitatively better for all phases of enhancement.

The $MC_{1\text{-min}}$ approach might be limited in cases for which the breathing pattern and the maximum breathing amplitude of a patient change considerably during the remaining PET acquisition. Moreover, when shortening the MR scan, the physiological signal would need to be derived by mean of an external device (e.g. respiratory belt) or using PET-based self-gating (*7,8*).

Finally, dedicated hardware and software are required for the PET and MR data processing and image reconstructions. In order to reduce the computational effort, the DCE-MRI reconstruction software was implemented using a fully 3D GPU-based NUFFT operator (*27*). The PET motion corrected reconstructions were also implemented using GPU-based projector and back-projector operators (*32*). A package containing the necessary software will be included in the GPU-based PET reconstruction toolbox (occiput.io (*32*)) and its specific implementation for the Biograph mMR will be provided to interested users upon request.

CONCLUSIONS

We presented and evaluated in vivo a comprehensive approach for self-gated MR motion modeling applied to respiratory motion compensation of PET and DCE-MRI data acquired simultaneously in an integrated PET/MR systems. Fully registered, motion corrected PET images and diagnostic DCE-MRI images were obtained with negligible acquisition time prolongation compared to standard breath-hold techniques. Both the MR and PET image quality and tracer uptake quantification were improved when compared to conventional methods. Furthermore, we demonstrated that respiratory motion correction of the PET data can also be performed based on the MR data acquired in 1 minute, allowing for more flexible PET/MR scanning protocols.

REFERENCES

1. Catana C, Guimaraes AR, Rosen BR. PET and MR imaging: the odd couple or a match made in heaven? *J Nucl Med.* 2013;54:815–824.

2. Martinez-Möller A, Eiber M, Nekolla SG, et al. Workflow and scan protocol considerations for integrated whole-body PET/MRI in oncology. *J Nucl Med.* 2012;53:1415–1426.

3. Catalano OA, Masch WB, Catana C, et al. An overview of PET/MR, focused on clinical applications. *Abdom Radiol.* 2017;42:631–644.

4. Li XA, Stepaniak C, Gore E. Technical and dosimetric aspects of respiratory gating using a pressure-sensor motion monitoring system. *Med Phys*. 2006;33:145–154.

5. Dawood M, Büther F, Lang N, et al. Respiratory gating in positron emission tomography: a quantitative comparison of different gating schemes. *Med Phys*. 2007;34:3067–3076.

6. Catana C. Motion Correction Options in PET/MRI. *Sem Nucl Med*. 2015;45:212–223.

7. Thielemans K, Rathore S, Engbrant F, Razifar P. Device-less gating for PET/CT using PCA. *Proc IEEE Nucl Sci Symp Med Imaging Conf*. 2011;3904–3910.

8. Fürst S, Grimm R, Hong I, et al. Motion correction strategies for integrated PET/MR. *J Nucl Med.* 2015;56:261–269.

9. McClelland JR, Hawkes DJ, Schaeffter T, et al. Respiratory motion models: a review. *Med Image Anal.* 2013;17:19–42.

10. King AP, Buerger C, Tsoumpas C, et al. Thoracic respiratory motion estimation from MRI using a statistical model and a 2-D image navigator. *Med Image Anal.* 2012;16:252–264.

11. Manber R, Thielemans K, Hutton BF, et al. Practical PET respiratory motion correction in clinical PET/MR. *J Nucl Med.* 2015;56:890–896.

12. Ozturk C, Derbyshire JA, McVeigh ER. Estimating motion from MRI data. *Proc IEEE.* 2003;91:1627–1648.

13. Chun SY, Reese TG, Ouyang J, et al. MRI-based nonrigid motion correction in simultaneous PET/MRI. *J Nucl Med.* 2012;53:1284–1291.

14. Würslin C, Schmidt H, Martirosian P, et al. Respiratory motion correction in oncologic PET using T1-weighted MR imaging on a simultaneous whole-body PET/MR system. *J Nucl Med.* 2013;54:464–471.

15. Guérin B, Cho S, Chun SY, et al. Nonrigid PET motion compensation in the lower abdomen using simultaneous tagged-MRI and PET imaging. *Med Phys.* 2011;38:3025–38.

16. Winkelmann S, Schaeffter T, Koehler T, et al. An optimal radial profile order based on the Golden Ratio for time-resolved MRI. *IEEE Trans Med Imaging.* 2007;26:68–76.

17. Buerger C, Clough RE, King AP, et al. Nonrigid motion modeling of the liver from 3-D undersampled self-gated golden-radial phase encoded MRI. *IEEE Trans Med Imag.* 2012;31: 805–815.

18. Grimm R, Fürst S, Souvatzoglou M, et al. Self-gated MRI motion modeling for respiratory motion compensation in integrated PET/MRI. *Med Image Anal*. 2015;19:110–120.

19. Chandarana H, Heacock L, Rakheja R, et al. Pulmonary nodules in patients with primary malignancy: comparison of hybrid PET/MR and PET/CT imaging. *Radiology.* 2013;268:874–881.

20. Chandarana H, Block TK, Rosenkrantz AB, et al. Free-breathing radial 3D fat-suppressed T1-weighted gradient echo sequence: a viable alternative for contrast-enhanced liver imaging in patients unable to suspend respiration. *Invest Radiol.* 2011; 46:648–653.

21. Feng L, Grimm R, Block KT, et al. Golden-angle radial sparse parallel MRI: combination of compressed sensing, parallel imaging, and golden-angle radial sampling for fast and flexible dynamic volumetric MRI. *Magn Reson Med.* 2014; 72:707–717.

22. Rank CM, Heußer T, Buzan MTA, et al. 4D Respiratory motion-compensated image reconstruction of free-breathing radial MR data with very high undersampling. *Magn Reson Med.* 2017;3:1170–1183.

23. Chandarana H, Feng L, Block KT, et al. Free-breathing contrast-enhanced multiphase MRI of the liver using a combination of compressed sensing, parallel imaging, and golden-angle radial sampling. *Invest Radiol.* 2013; 48:10–16.

24. Pang J, Sharif B, Fan Z, et al. ECG and navigator-free 4D whole-heart coronary MRA for simultaneous visualization of cardiac anatomy and function. *Magn Reson Med*. 2014;72:1208–1217.

25. Feng L, Axel L, Chandarana H, et al. XD-GRASP: Golden-angle radial MRI with reconstruction of extra motion-state dimensions using compressed sensing. *Magn Reson Med.* 2016;75:775–788.

26. Fessler A, Sutton BP. Nonuniform fast Fourier transforms using min-max interpolation. *IEEE Tran Sign Proc.* 2003;51:560–574.

27. Knoll F, Schwarzl A, Sodickson DK, et al. gpuNUFFT - An Open-Source GPU library for 3-D gridding with direct Matlab interface. *Proc ISMRM.* 2014;42:97–4308.

28. Klein S, Staring M, Pluim JPW, et al. elastix: A toolbox for intensity-based medical image registration. *IEEE Tran Med Imag*. 2010;29:196–2015.

29. Hudson HM, Larkin RS. Accelerated image reconstruction using ordered subsets of projection data. *IEEE Trans Med Imag.* 1994;13:601–609.

30. Lamare F, Ledesma Carbayo MJ, Visvikis D et al. List-mode-based reconstruction for respiratory motion correction in PET using non-rigid body transformations. *Phys Med Biol*. 2007;52:5187–5204.

31. Reader AJ, Verhaeghe J. 4D image reconstruction for emission tomography. *Phys Med Biol.* 2014;59:371–418.

32. Pedemonte S, Fuin N. Occiput.io (accessed October 10, 2017).

33. Kinahan PE, Karp JS. Figures of merit for comparing reconstruction algorithms with a volume-imaging PET scanner. *Phys Med Biol*. 1994;39:631–642.

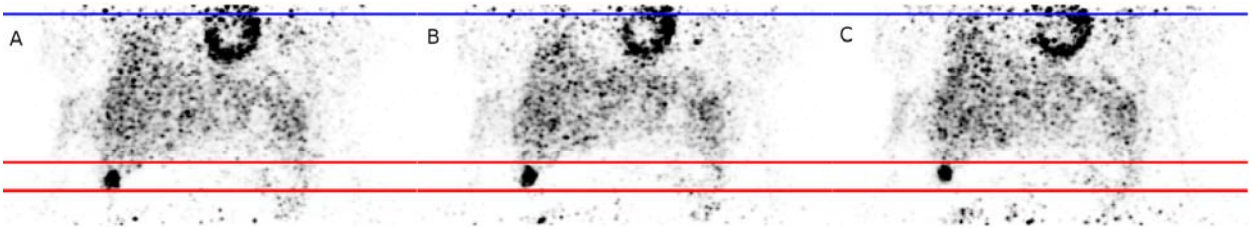

Figure 1: PET reconstructions for different respiratory gates, showing a coronal slice through a lesion in the liver of patient 1. Fig. 1A shows an end-of-inspiration motion phase; Fig. 1B shows an intermediate phase; and Fig. 1C shows an end-of-expiration phase.

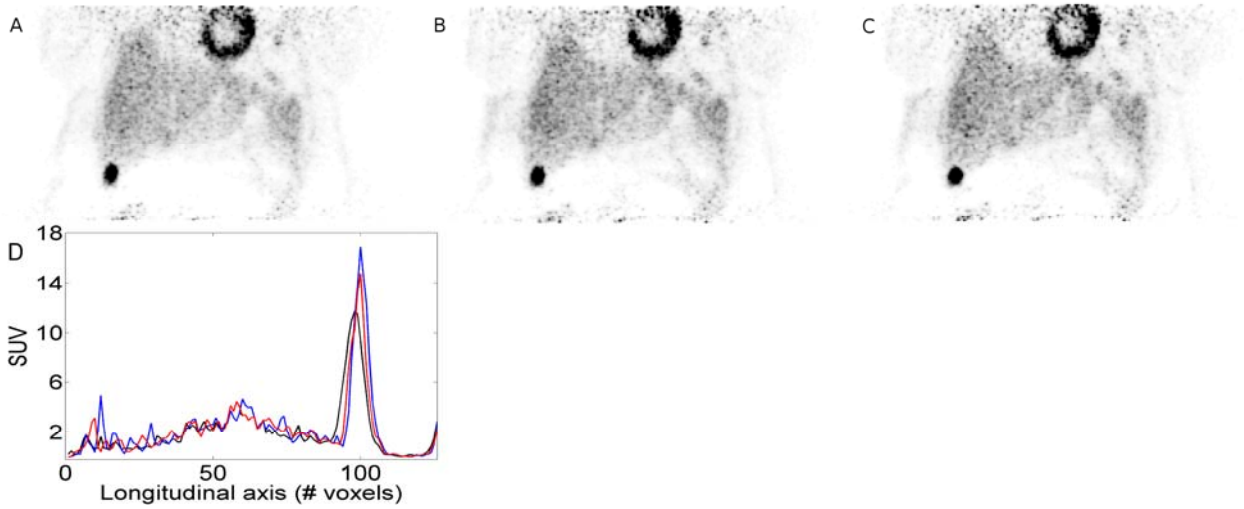

Figure 2: Comparison of uncorrected (A), $MC_{1\text{-min}}$ (B) and $MC_{6\text{-min}}$ (C) PET reconstructions for patient 1; showing the coronal slice presented in Fig. 1. The plots in Fig. 2D show line profiles through the lesion for the three reconstructions methods: black - non motion-corrected; red - $MC_{1\text{-min}}$; and blue - $MC_{6\text{-min}}$.

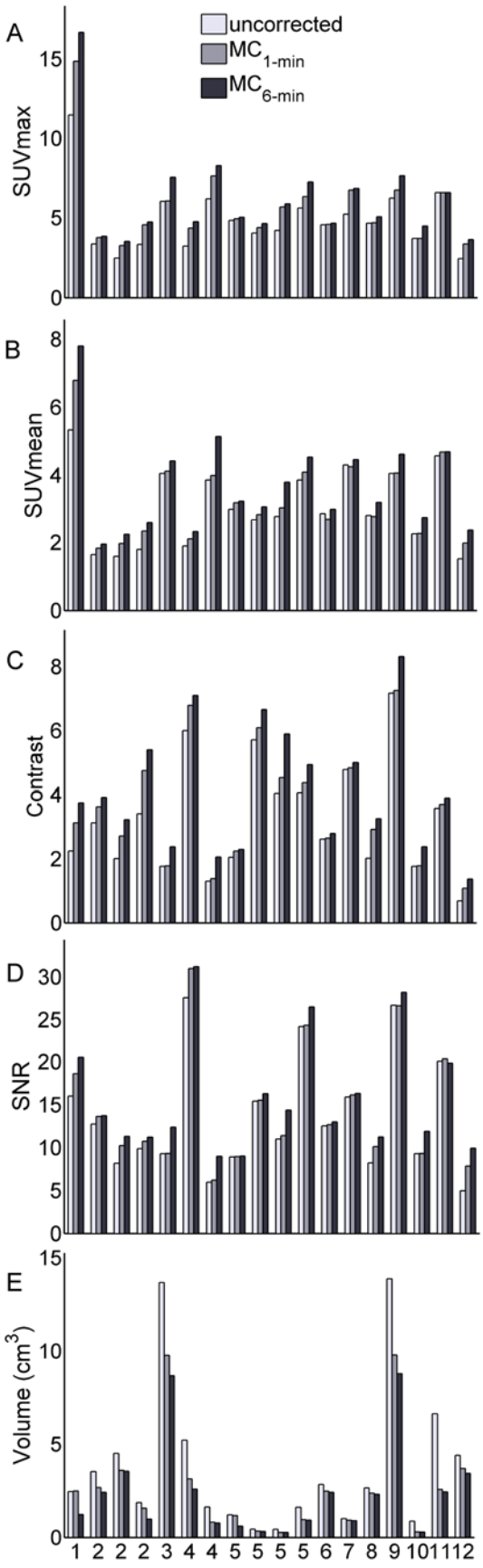

Figure 3: Bar charts representing the figures of Merit for the quantification of motion-compensation accuracy for $MC_{1\text{-}min}$ and $MC_{6\text{-}min}$ protocols with respect to non-motion corrected PET images. Fig. 3A shows differences in SUVmax, Fig. 3B shows differences in SUVmean, Fig. 3C shows differences in Contrast, Fig. 3D shows differences in SNR and Fig. 3E shows differences in lesion volume (in cm^3).

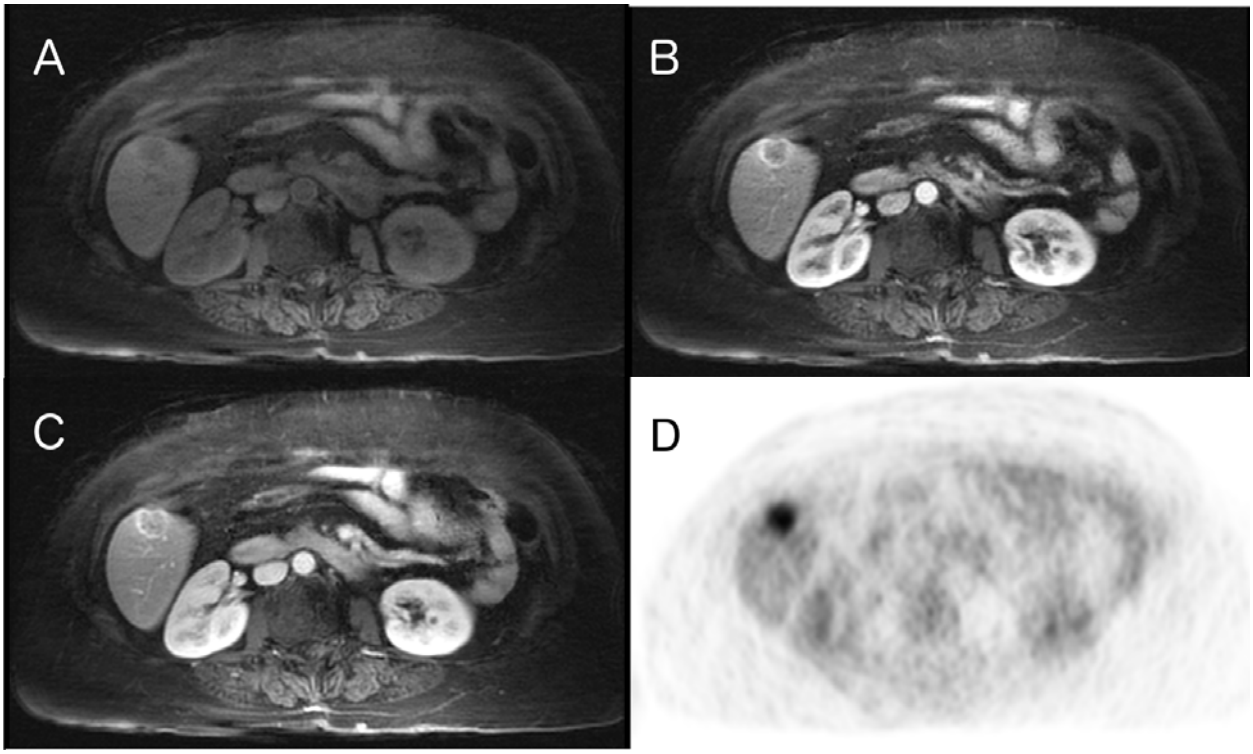

Figure 4: DCE-MRI images of the liver using moco_GRASP reconstruction (A,B,C), together with the corresponding motion-corrected PET image (Fig. 4D), showing an axial slice through a lesion in the liver of patient 1. Fig. 4A shows the non-contrast enhanced phase, Fig. 4B the arterial dominant phase, Fig. 4C shows the portal venous phase, and Fig. 4D shows the corresponding motion-corrected PET image.

TABLE 1 - MSE for the different reduced scan times and for the different reconstruction methods, with respect to the full 6 min acquisition using GRASP reconstruction.

Patient #	**6 min invFFT**	**1 min invFFT**	**1 min GRASP**
1	219	2073	956
2	178	1413	463
3	184	1666	287
4	155	1162	218
5	221	1845	489
6	165	1940	938
7	205	1172	309
8	147	1210	256
9	179	1751	429
10	134	1202	293
11	222	1804	460
12	178	1399	483

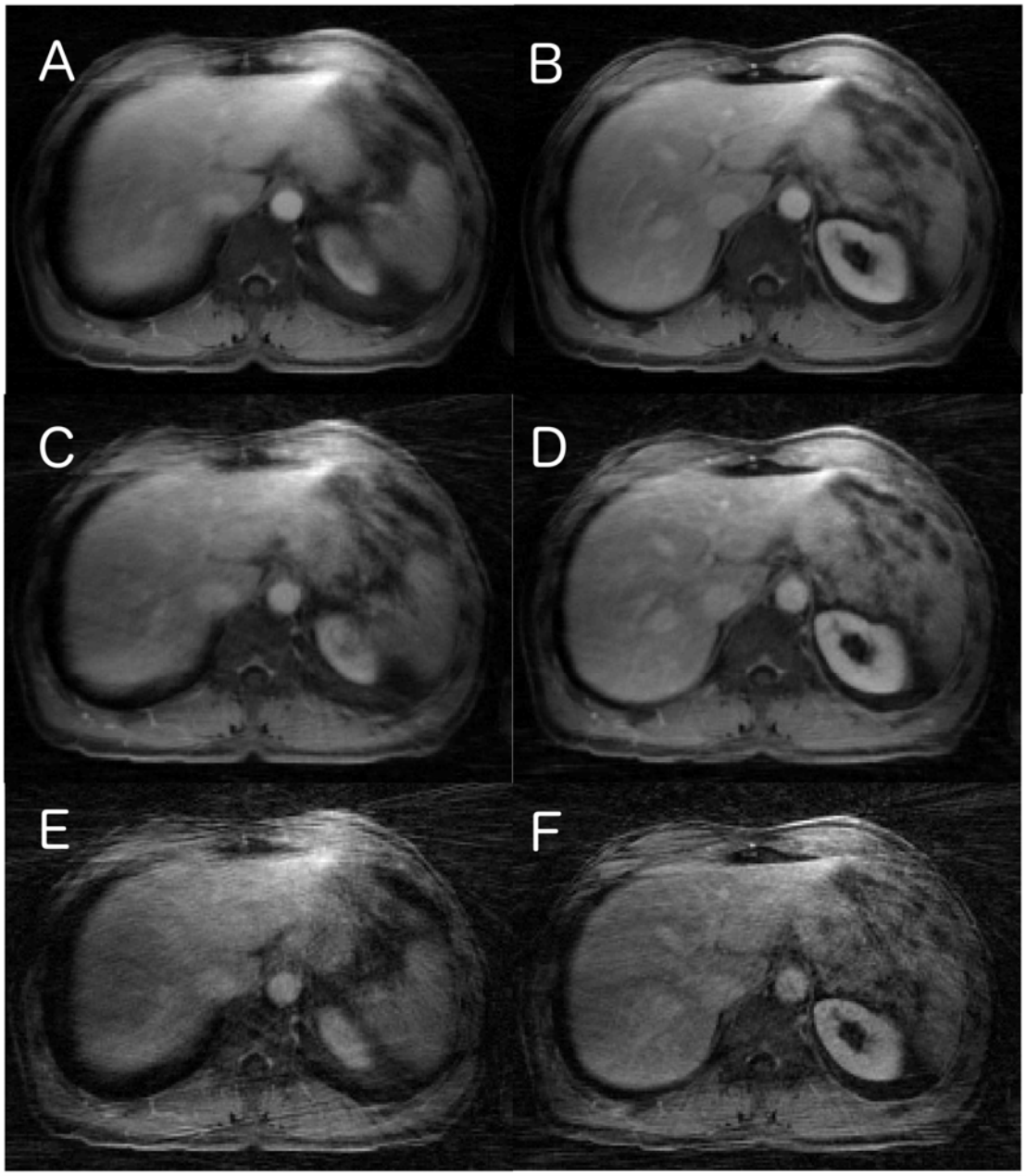

Supplemental Figure 1: MRI images for the end-of-inspiration (A,C,E) and end-of-expiration (B,D,F) respiratory phases for patient 1. Supplemental Figs. 1A and 1B a 6 min radial_VIBE acquisition using GRASP reconstruction ($MC_{6\text{-min}}$); C,D show a 1 min radial_VIBE acquisition using GRASP reconstruction ($MC_{1\text{-min}}$); and Supplemental Figs. 1E and 1F show show a 1 min radial_VIBE acquisition using non-iterative reconstruction ($MC_{1\text{-ifft}}$).

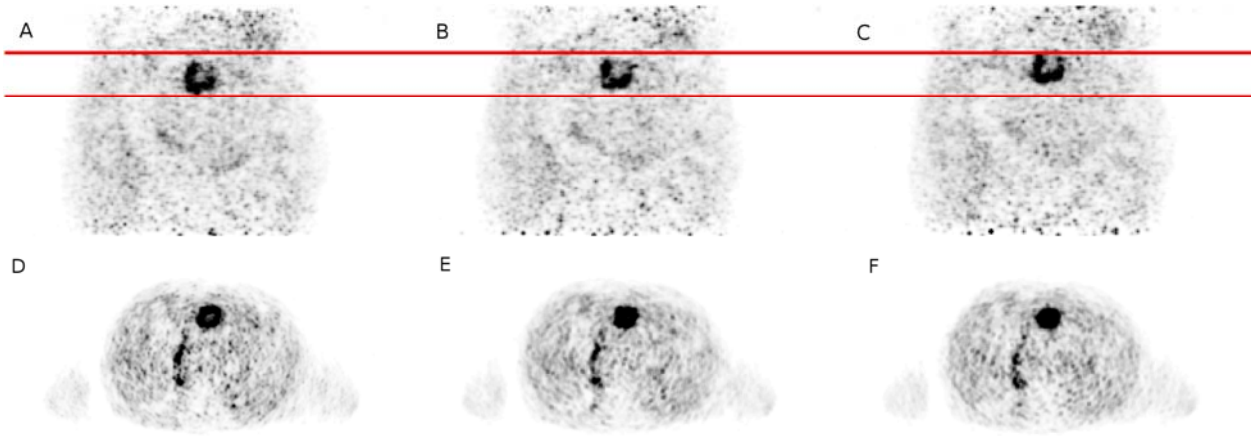

Supplemental figure 2: PET reconstructions for different respiratory gates, showing a coronal slice (A,B,C) and an axial slice (D,E,F) through a lesion in the liver of patient 8. Supplemental Figs. 1A and 1D show an end-inspiration motion phase; Supplemental Figs. 1B and 1E show an intermediate phase; and Supplemental Figs. 1C and 1F show an end-of-expiration phase.

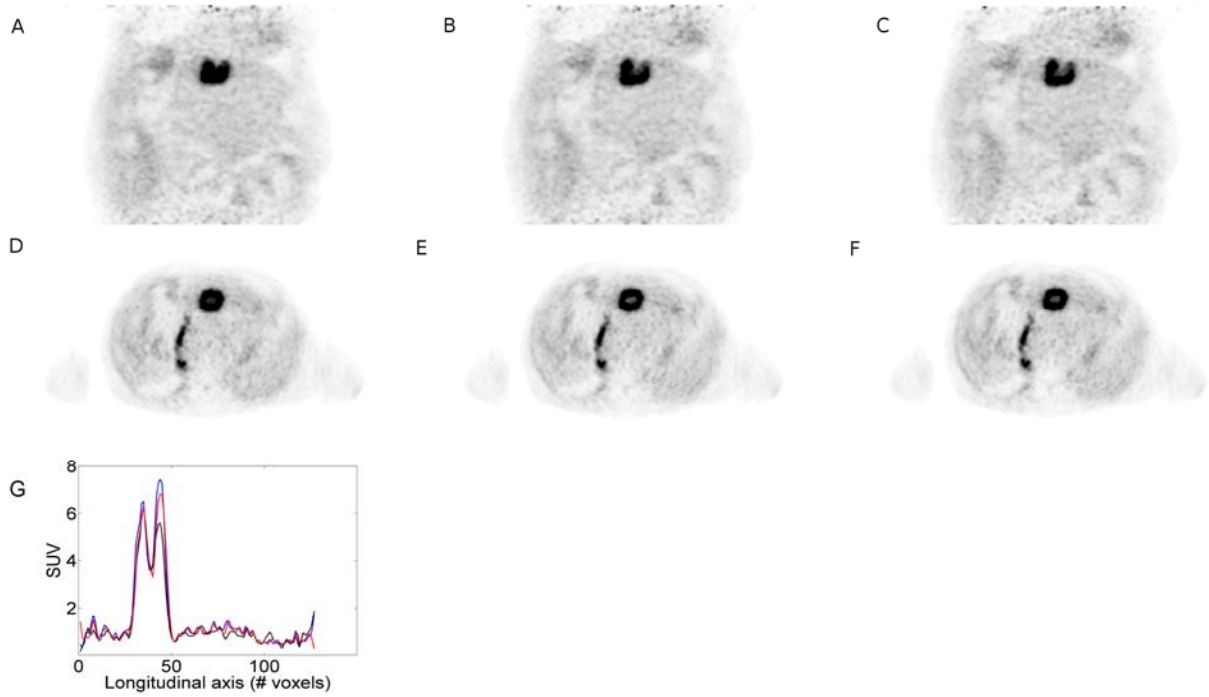

Supplemental figure 3: Comparison of uncorrected (A,D), $MC_{1\text{-}min}$ (B,E) and $MC_{6\text{-}min}$ (C,F) PET reconstructions for patient 8; showing the coronal slice presented in Supplemental Fig. 2. The plots in Supplemental Fig. 2G show line profiles through the lesion for the three reconstructions methods: black - non motion-corrected; red - $MC_{1\text{-}min}$; and blue - $MC_{6\text{-}min}$.

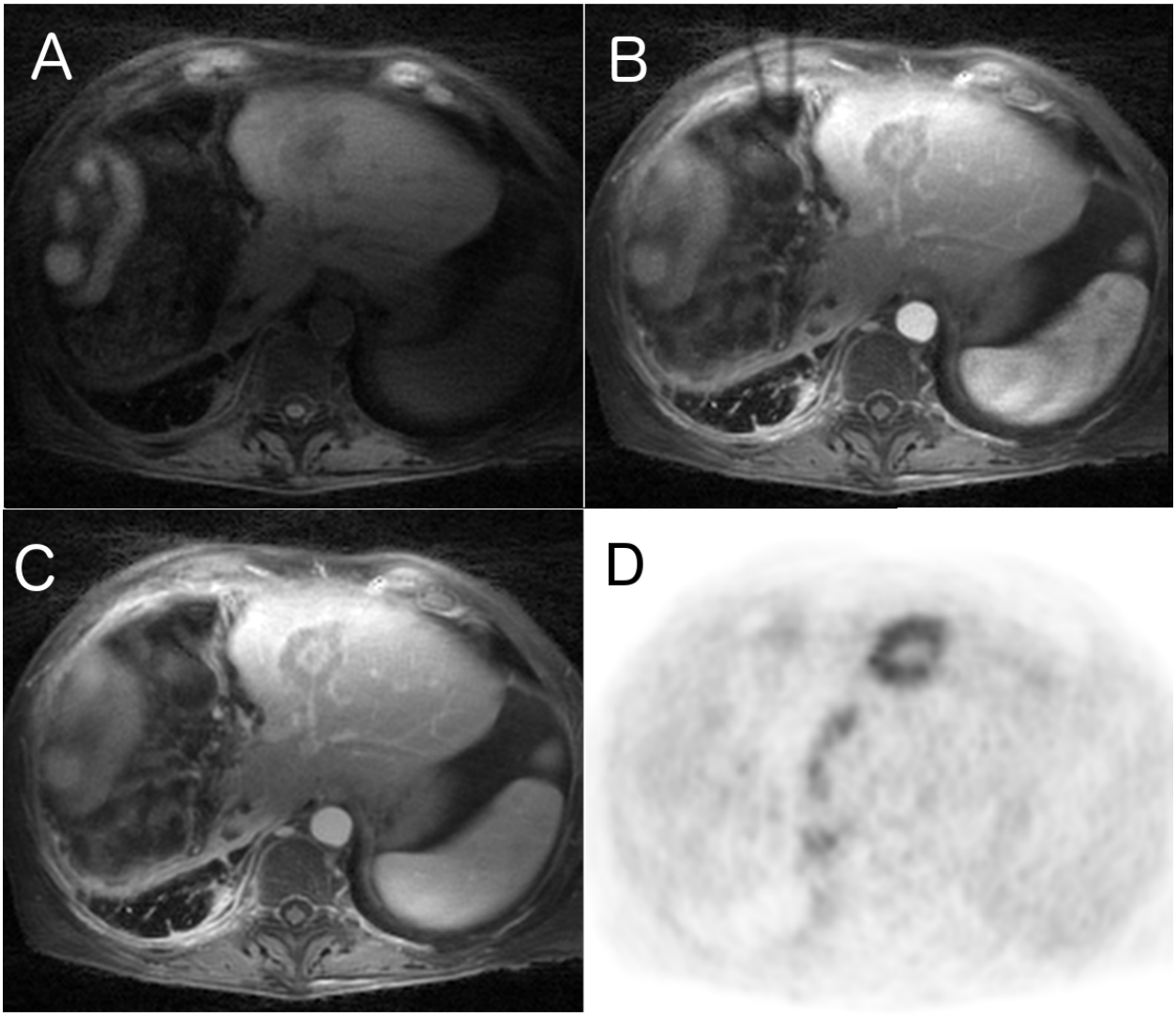

Supplemental figure 4: DCE-MRI images of the liver using moco_GRASP reconstruction (A,B,C), together with the corresponding motion-corrected PET image (D), showing an axial slice through a lesion in the liver of patient 8. Supplemental Fig. 3A shows the non-contrast enhanced phase, Supplemental Fig. 3B shows the hepatic arterial dominant phase, and Supplemental Fig. 3C shows the portal venous phase.

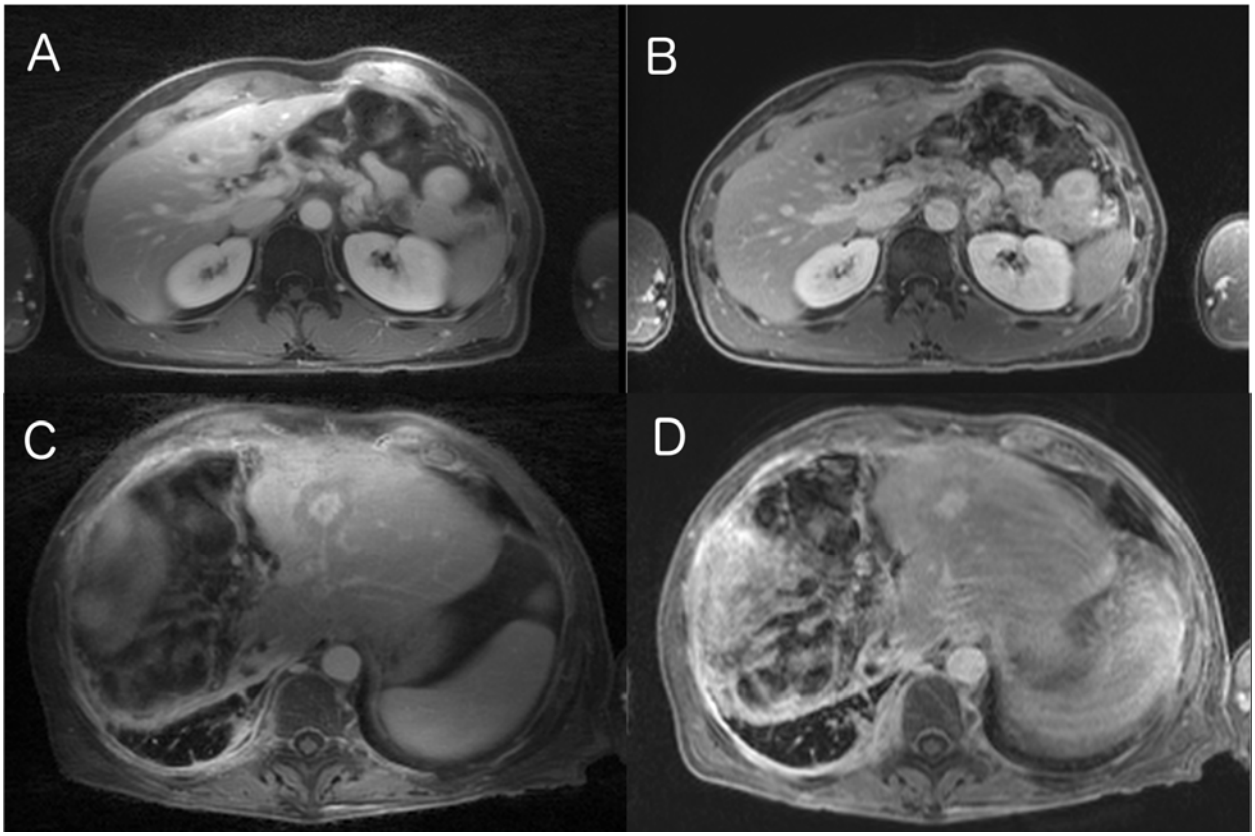

Supplemental figure 5: Comparison of late phase of DCE-MRI images obtained from radial_VIBE acquisitions using the moco_GRASP reconstruction method (A,C), and from cartesian bh_VIBE acquisitions (B,D). Supplemental Figs. 4A and 4B show an axial slice through the liver of patient 4 and Supplemental Figs. 4C and 4D show an axial slice through a lesion in the liver of patient 8.